Frontiers in Heat
and Mass Transfer

Tech Science Press

https://doi.org/10.32604/fhmt.2026.079549

ARTICLE

Mechanism of Wettability–Rough Morphology Coupling on Convective Heat Transfer in Nanochannels

Yanfeng Li[1,2], **Xiaohui Zhang**[1,2,*], **Luyang Chen**[3,*], **Rong Chen**[4] **and Shan Qing**[3]

[1]State Key Laboratory of Complex Nonferrous Metal Resources Clean Utilization, School of Metallurgical and Energy Engineering, Kunming University of Science and Technology, Kunming, China
[2]Yunnan Key Laboratory of Clean Energy and Energy Storage Technology, School of Metallurgical and Energy Engineering, Kunming University of Science and Technology, Kunming, China
[3]School of Metallurgical and Energy Engineering, Kunming University of Science and Technology, Kunming, China
[4]School of Mechanical and Electrical Engineering, Yunnan Agricultural University, Kunming, China

*Corresponding Authors: Xiaohui Zhang. Email: xiaohui.zhang@kust.edu.cn; Luyang Chen. Email: lychen@kust.edu.cn

Received: 23 January 2026; Accepted: 04 March 2026; Published: 29 June 2026

ABSTRACT: Highly integrated micro-nano electronic devices suffer from severe heat dissipation challenges, and flow cooling in nanochannels is an effective solution. During convective heat transfer at liquid-solid interfaces, surface wettability and rough morphology are key parameters governing thermal transport; however, their combined effects remain unclear. In this study, molecular dynamics simulations are utilized to examine the synergistic effects of surface wettability and nanopillar arrays on thermal transport and fluid dynamics within nanochannels. The results show that increasing surface hydrophilicity and roughness reduces the thermal slip length and increases the Nusselt number, thereby enhancing heat transfer performance in the nanochannel. From a fluid dynamics standpoint, velocity slip length decreases while the relative friction coefficient increases, signifying greater flow resistance. For the present model, the enhancement in heat transfer induced by increased wettability is significantly greater than that caused by increased roughness, whereas their effects on flow resistance are difficult to distinguish the dominance. At the microscale, increased wettability and roughness facilitate the accumulation of fluid atoms near the liquid-solid interface. The elevated interaction energy between solid platinum atoms and fluid argon atoms is identified as the primary mechanism underlying thermal transport enhancement in nanochannels. This investigation offers valuable insights for the optimized thermal management of micro-nano electronic devices.

KEYWORDS: Nanochannel; nanopillar arrays; heat transfer; flow resistance; molecular dynamics

1 Introduction

The increasing integration of micro-nano electronic devices drives a pressing need for more efficient heat dissipation [1]. Enhancing convective heat transfer at the micro-nano scale is a key approach to addressing thermal management challenges. therefore, an increasing number of scientists are focusing on improving the convective heat transfer process of micro-nano channels [2–5]. Unlike conventional macroscopic systems, molecular interactions dominate fluid flow and heat transfer at micro-nano scales. Factors neglected at the macroscopic scale must be reconsidered, including fluid compressibility, interfacial thermal resistance, thermal slip, and velocity slip [6]. At present, studies on convective heat transfer in micro-nano channels mainly focus on microscale channels, whereas investigations of nanochannels remain limited, primarily due to the difficulty of experimentally measuring parameters within nanochannels using conventional techniques. Rooted in classical Newtonian mechanics to describe particle motions, molecular dynamics (MD) simulation has played an instrumental role in recent scientific efforts to elucidate flow and heat transfer mechanisms in nanochannels [7–9].

In 2005, Markvoort et al. [10] first proposed a nanochannel convective heat transfer model based on the MD method. Their study demonstrated that solid–liquid interactions play a crucial role in heat transfer characteristics, and hydrophilic surfaces are more favorable for enhancing heat transfer between nanochannel walls and the fluid. In the same year, Ge et al. [11] improved the model proposed by Markvoort et al. by rearranging the temperature control region and the external force region, thereby enabling precise control of the fluid inlet temperature. At present, most MD simulations of nanochannel heat transfer are based on the model developed by Ge et al. Convective heat transfer performance in nanochannels is governed by a multitude of factors, including surface wettability [12–14], surface nanostructures [15–17], and channel size [18,19]. Velocity slip is defined as the tangential velocity discrepancy between the working fluid and the solid boundary at the liquid-solid interface during channel flow. In convection systems at the nano scale, the slip length is comparable to the characteristic length scale of the system. therefore, velocity slip cannot be neglected and significantly affects nanoscale convection behavior [20,21]. Using MD simulations, Toghraie Semiromi and Azimian [22] studied liquid argon flow in nanochannels and revealed that the interfacial slip length is positively correlated with the applied driving force. In 1941, Kapitza [23] discovered and introduced the concept of interfacial thermal resistance at the interface between liquid helium and solid walls. Interfacial thermal resistance is defined as the ratio of the interfacial thermal slip to the heat flux per unit area per unit time. Ma et al. [24] studied the interfacial thermal conductance between silica and water and reported that increased wettability leads to a higher average number of hydrogen bonds in water molecules, inducing structural changes in the interfacial water layer and thereby enhancing interfacial heat transport. With respect to surface roughness, Lin et al. [25] showed that rough nanostructures can reduce interfacial thermal resistance. Rashidi et al. [15] investigated the effect of rough surfaces on the condensation rate and the number of atoms causing liquid phase movement. The results show that the condensation flow rate in rough nanochannels depends on the geometry and height of the roughness, so by increasing the roughness height, the flow is more significantly affected. Zhang et al. [26] developed a model for pressure-driven flow in nanochannels with inward/outward semicircular surface roughness. Their study showed that inward roughness increased flow resistance, reduced velocity, and led to local ion accumulation, whereas outward roughness caused only minor flow disturbances, with ions accumulating within the rough structures. Li et al. [27] found that fluid flow has little effect on the interfacial thermal resistance of atomically smooth channels, but reduces it in rough channels. This difference is attributed to variations in the flow and temperature fields. Rough morphology disturbs the parallel flow of the fluid and suppresses thermal vibrations of the interfacial fluid.

The question of whether the combined effect of wall wettability and roughness on nanochannel heat transport resembles the outcome of a single variable has drawn interest from researchers. Song et al. [9] constructed a flow simulation framework incorporating varied wall wettability levels and rough surface topographies; their findings indicated that elevated wall wettability and surface roughness strengthen thermal exchange between the solid boundary and the fluid. Miao et al. [28] used MD simulations to investigate liquid argon flow and heat transfer in nanochannels with random roughness, demonstrating that both surface wettability and rough structure significantly affect temperature distribution, thermal slip, flow resistance, and velocity slip. Yao et al. [29] reported that rough morphologies are responsible for enhanced heat conduction and flow resistance, originating from the restriction of fluid atom motion by nanostructured grooves. In contrast, strong solid–liquid interactions improve heat conduction while increasing flow resistance, which is attributed to enhanced interfacial adsorption. Qin et al. [30] employed water as the working fluid and established a coupled model of nanostructures and wall wettability, attributing the enhancement of heat transfer to increases in fluid density, hydrogen bond number, and solid–liquid interaction energy. Nanopillar arrays, as a form of surface roughness, exhibit excellent thermal conduction performance [31,32]. However, they have not yet been investigated in nanochannel convective heat transfer simulations. In the above studies, most works lack a systematic analysis of the extent to which roughness enhance heat transfer while affecting flow resistance. Moreover, the mechanism by which wall wettability coupled with nanopillar array roughness influences the overall heat transfer performance in nanochannels remains unclear.

In this study, nanopillar arrays are introduced on nanochannel surfaces to modify wall roughness. Four nanopillar array surfaces under strong and weak wettability conditions are designed to construct a coupled model of surface nanostructures and wall wettability. The results indicate that, for the present model, heat transfer is dominated by wettability, whereas flow resistance exhibits an inconsistency between wettability and roughness effects. Nanopillar arrays significantly enhance heat transfer while relatively avoiding excessive suppression of fluid flow.

2 Calculation Model and Method

2.1 Model Construction and Simulation Parameters

The simulation model (Fig. 1) features a nanochannel filled with argon atoms at a density of 1.2 g/cm^3. The walls are represented by six layers of platinum atoms per side, arranged in a face-centered cubic (FCC) structure with a lattice constant δ of 3.923 Å. Argon atoms with an average density of 1.2 g/cm^3 are used as the working fluid. The simulation box dimensions are $L_x = 100 \times \delta$, $L_y = 15 \times \delta$, and $L_z = 37 \times \delta$ ($X^* = L_x/\delta$, $Y^* = L_y/\delta$, $Z^* = L_z/\delta$), and the thickness of each wall is 3δ. The two outermost platinum atomic layers at the system boundaries were designated as stationary boundary regions to mitigate structural deformation within the simulation domain, whereas the remaining platinum atoms were assigned the role of thermal sources and regulated via a Langevin thermostat. Periodic boundary conditions were implemented along the x and y axes, whereas non-periodic boundary conditions were adopted along the *z* axis. Arrays of nanopillar arrays were patterned on the channel walls, as depicted in Fig. 2, and the detailed parameters of the four roughness cases are listed in Table 1.

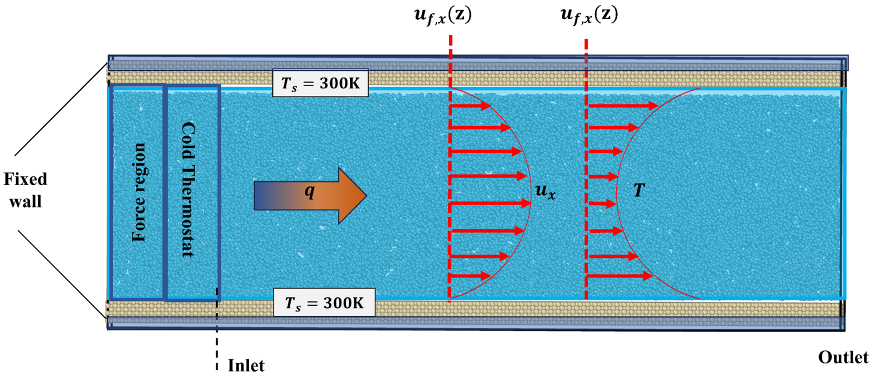

Figure 1: Schematic diagram of simulation system.

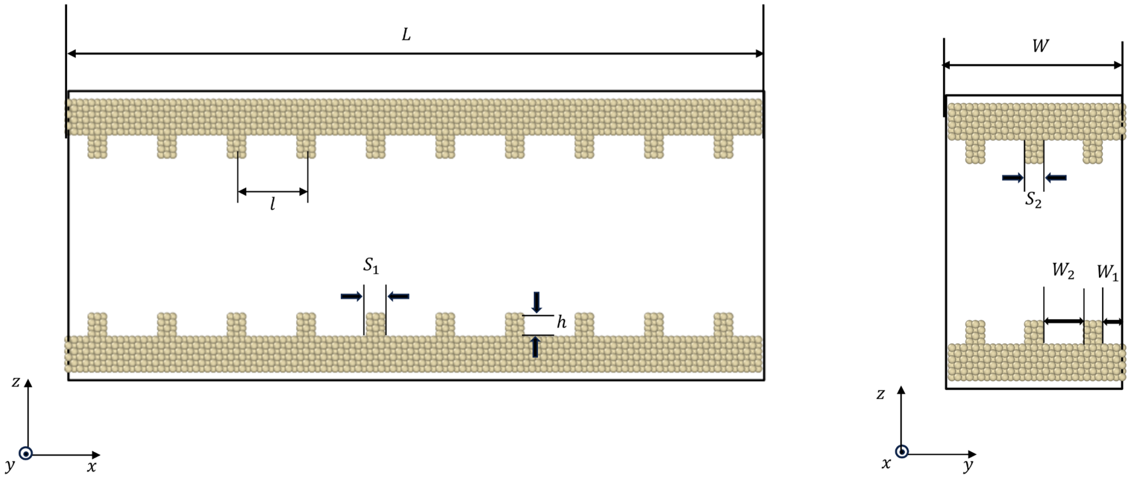

Figure 2: Schematic diagram of surface roughness structure of nanochannel (nanopillar array).

Table 1: Geometric parameters of nanopillar arrays under different roughness conditions.

Particle	S_1	S_2	l	h	W_1	W_2
Case 1	/	/	/	/	/	/
Case 2	1.5δ	1.5δ	15δ	2δ	5δ	2.5δ
Case 3	1.5δ	1.5δ	10δ	2δ	5δ	2.5δ
Case 4	1.5δ	1.5δ	7δ	2δ	5δ	2.5δ

Fig. 1 illustrates that the computational domain along the x-axis is partitioned into three distinct segments: a force application region, a temperature resetting zone, and a data collection region. The force application segment spans from 0 to 3δ along the x-axis, where a steady force of 1.2 pN is exerted on the argon atoms. The temperature resetting region spans from 3δ to 6δ along the x direction. Within this zone, argon atoms undergo temperature resetting and are maintained at 200 K via thermostatting, without disturbing the flow direction. The region from 6δ to 100δ along the x-direction is defined as the data acquisition region, where temperature and velocity data are collected for analysis.

This study performs MD simulations based on the LAMMPS software package [33]. The 12–6 Lennard-Jones (L-J) potential is employed to describe Pt–Pt and Ar–Ar interactions [17]. For the Pt–Ar interaction, the Lorentz–Berthelot mixing rules are employed. The cutoff distance is set to 0.1 nm. The interaction strength between platinum and argon is adjusted by varying α, thereby tuning the wettability of the platinum surface. Wettability is characterized by the contact angle. To adjust the wettability of the platinum surface, weak wettability is defined as a contact angle of 68.5° at $\alpha = 0.5$, and strong wettability is defined as a contact angle of 18.4° at $\alpha = 1$.

$$\phi(r) = 4\alpha\varepsilon\left[\left(\frac{\sigma}{r}\right)^{12} - \left(\frac{\sigma}{r}\right)^{6}\right] \tag{1}$$

In the equation, ε is the energy parameter, α is the adjustment factor for regulating the coupling strength between Pt and Ar, σ is the distance parameter, and r denotes the interatomic distance. The Lennard-Jones (L-J) potential parameters employed for the atomic interactions in this study are listed in Table 2.

Table 2: L-J parameters for Pt–Ar solid–liquid interactions.

Particle	ε (ev)	σ (nm)
Pt-Pt	0.521	2.475
Ar-Ar	0.0104	3.405
Pt-Ar	0.074	2.940

2.2 Simulation Details

The computational simulation workflow proceeds as outlined below. (1) Energy minimization is first performed to obtain a stable initial configuration. (2) The simulation was performed within the canonical (NVT) ensemble, with the system temperature controlled at 300 K by a thermostat over a period of 1 ns. (3) Subsequently, atoms in the boundary regions are fixed, and the system is switched to the microcanonical (NVE) ensemble. A Langevin thermostat is employed to regulate the temperatures of the heat source region and temperature resetting region to 300 and 200 K, respectively, while a constant driving force is applied to atoms in the force region for a duration of 3 ns. (4) Ultimately, the system is operated for 4 ns under the NVE ensemble to facilitate data collection. The simulation time step is set to 1 fs, with atomic positions updated via the standard velocity-verlet algorithm [34]. The simulation domain is divided into 100 bins along the x direction and 37 layers along the z direction, resulting in grid cells of size $\delta \times 15\delta \times \delta$ (x × y × z). Fluid properties within each cell are recorded to analyze heat transfer and flow behavior in the nanochannel. Simulation data are output every 1000 time steps, and visualization of atomic trajectories was performed using the open visualization software VMD [35].

3 Results and Discussion

3.1 Effect of Wettability and Rough Morphology Coupling on Temperature Characteristics in Nanochannels

To examine the synergistic impact of wettability and rough morphology on thermal transport within nanochannels, two-dimensional temperature profiles along the flow direction across various simulation models are illustrated in Fig. 3. Under all models, the fluid temperature increases in the force region and is then reset to 200 K in the temperature resetting region. In the data acquisition region, the fluid exchanges heat with the high-temperature walls. The low-temperature zone near the outlet is caused by axial heat conduction, which is consistent with previous studies [36,37]. For the same roughness configuration, the fluid temperature in strongly wetting nanochannels is significantly higher than that in weakly wetting ones. This is attributed to stronger adsorption of fluid atoms by solid atoms, which promotes more effective heat exchange. For the same wettability, higher wall roughness leads to more pronounced fluid temperature development. The increased number of nanopillar arrays enlarges the solid–fluid contact area, enhances atomic collisions, and facilitates efficient energy transfer between solid and fluid atoms at the interface. Notably, Case $4-\alpha=1$ exhibits the largest high-temperature region, indicating the most developed temperature field. This demonstrates that increasing both wettability and interfacial roughness is beneficial for heat exchange in nanochannels.

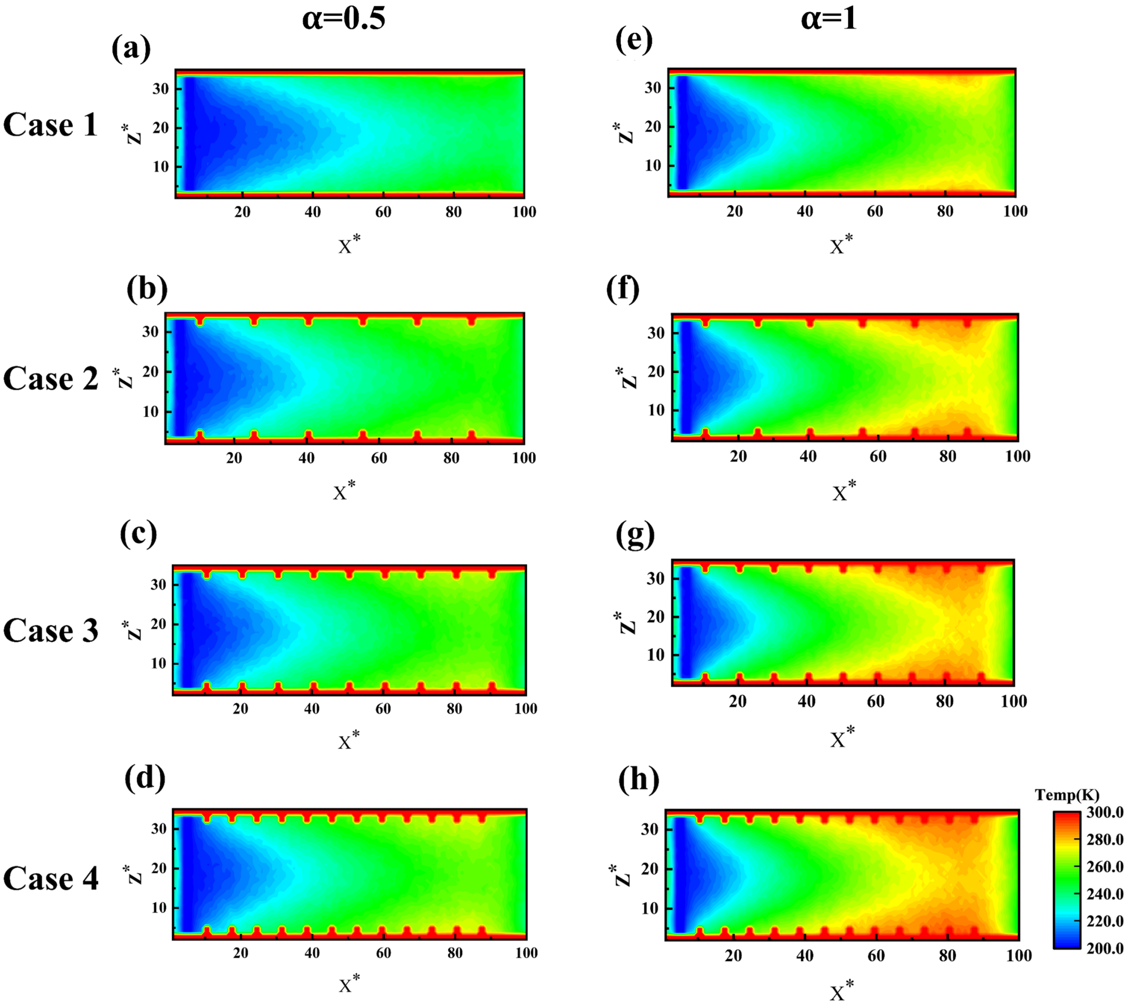

Figure 3: Two-dimensional temperature distributions; (**a**–**h**) nanochannels with different roughness and wettability.

Fig. 4 presents the one-dimensional temperature distributions along the *z* direction at different x positions. At X* = 6, the temperatures of all models are mainly within 200–205 K, indicating effective temperature control in the temperature resetting region. Since heat is transferred from the high-temperature walls to the low-temperature fluid, the maximum fluid temperature appears near the wall. The highest temperature in Case 1 − α = 4 is approximately 292 K, which is the largest among all models. The maximum temperature in Case 1 − α = 1 is about 280 K, which is even higher than that of Case 4 − α = 0.5 (271 K). The temperature distributions along the *z* direction at X* = 85.5 for all models are shown in Fig. 5a. At the same cross-section, the lowest temperature distribution is observed in the weakly wetting smooth nanochannel, whereas the highest temperature distribution occurs in the strongly wetting nanochannel with the largest roughness. Combined with Fig. 3, it can be concluded that, in this study, the effect of wettability on heat transfer is much more significant than that of wall roughness.

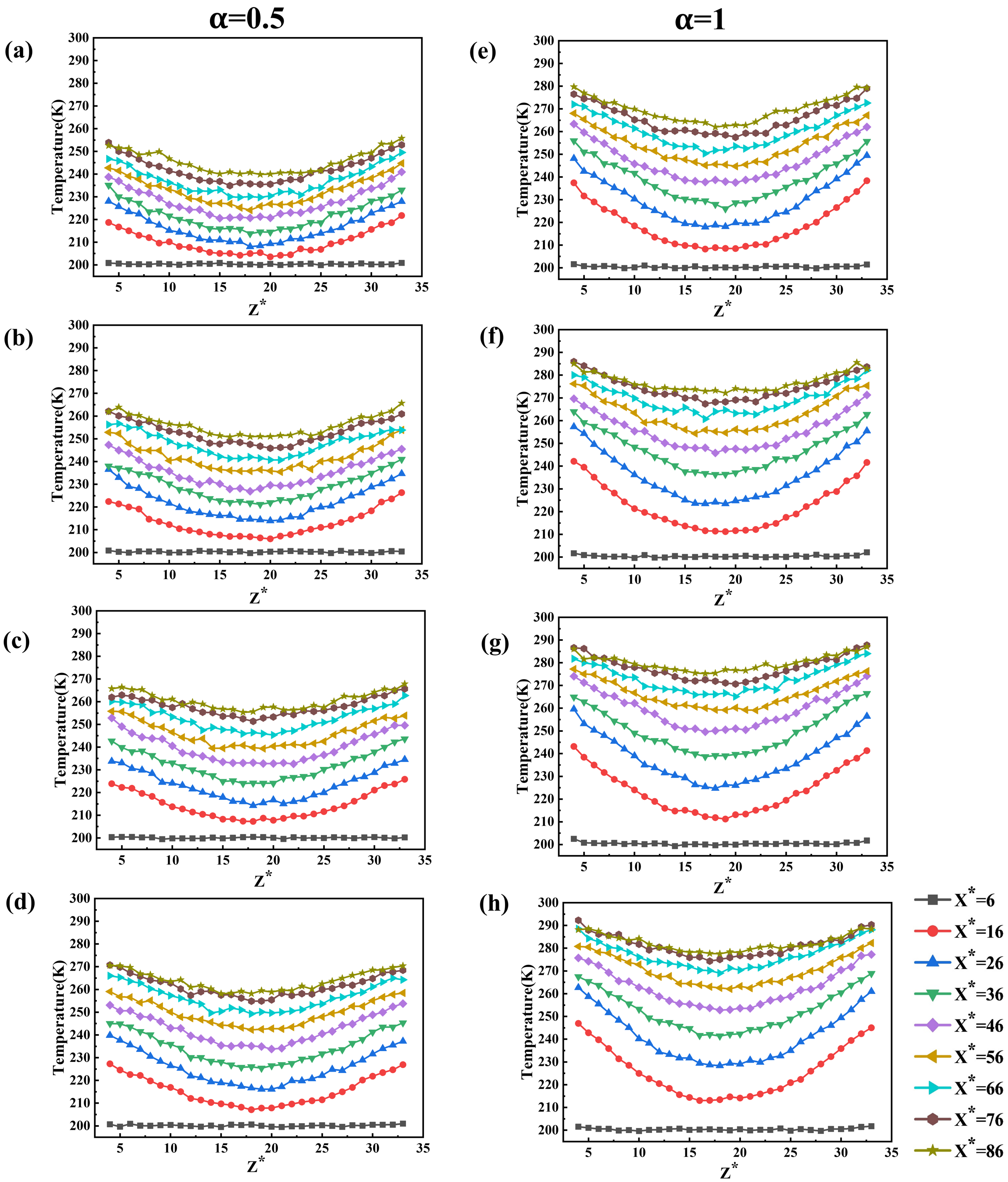

Figure 4: Temperature distributions along the *z* direction at different x positions; (**a**–**h**) nanochannels with different roughness and wettability.

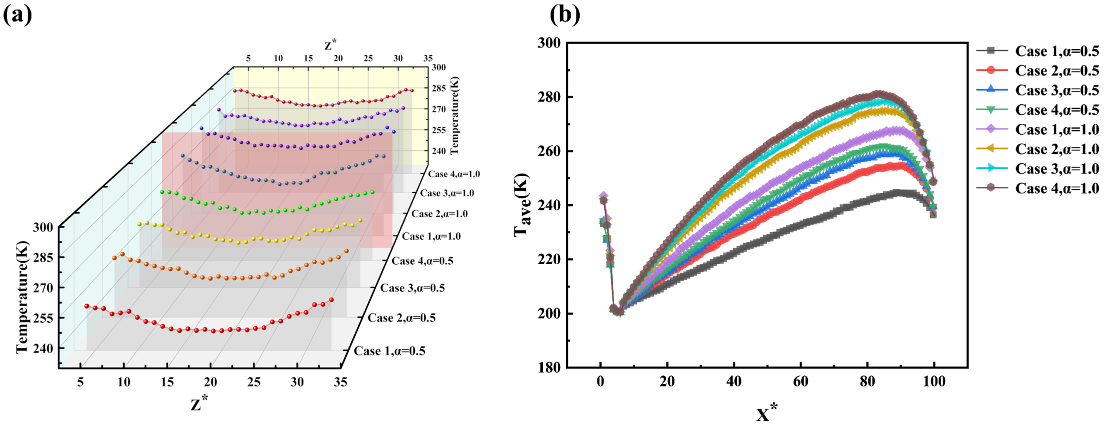

Figure 5: (**a**) Temperature distributions of different models at X* = 85.5; (**b**) local average temperatures of different models.

To investigate the fluid temperature variation along the flow direction, the local average fluid temperature in this direction, denoted as T_{ave}, is defined. Its calculation formula is given as follows [38]:

$$\mathrm{T}_{ave}\left(x\right)=\frac{\int_0^H c_p\rho u_x\left(x,z\right)T\left(x,z\right)dz}{\int_0^H c_p\rho u_x\left(x,z\right)dz} \tag{2}$$

In the equation, 0 and H denote the lower and upper boundaries of the fluid region in the nanochannel, respectively. c_p is the specific heat capacity of the fluid and is assumed to be constant. p is the fluid density, while $u_x\left(x,z\right)$ and $T\left(x,z\right)$ represent the local average velocity and temperature of the fluid, respectively.

The results are shown in Fig. 5b. Owing to the applied constant driving force, the average temperature near the inlet of the nanochannel is much higher than 200 K, which highlights the necessity of temperature resetting. From X* = 6 to X* = 90, the local average temperature develops along the flow direction. A temperature decrease is observed in the region from X* = 90 to X* = 100, which is caused by axial heat conduction. The highest local average temperature is obtained for Case 4 − α= 1, followed by Case 3 − α = 1 and 4 − α = 1, which is consistent with the previous discussion. Clearly, as the nanochannel surface exhibits greater hydrophilicity and the density of surface nanopillar arrays rises, the locally averaged temperature along the flow direction evolves more substantially and attains higher peak temperatures. This indicates improved temperature field development and enhanced heat transfer within the nanochannel.

As shown in Figs. 4 and 5a, the temperature difference between the fluid and the wall appears at the solid–liquid interface. To quantitatively investigate the correlation between this temperature discrepancy and interfacial thermal resistance, the thermal slip length (l_k) is introduced to describe the thermal slip response of the fluid. The corresponding definition is given in Eq. (8) [39]. The Nusselt (Nu) number is utilized to assess the magnitude of convective thermal transport within the nanochannel, with values computed via Eq. (5) [40], here, $h(x)$ represents the local convective heat transfer coefficient derived from Eq. (4). The calculation range for both Nu number and l_k is selected from X* = 45 to X* = 85.

$$Nu=\frac{h\left(x\right)D_h}{\lambda} \tag{3}$$

$$h\left(x\right)=\frac{\lambda}{\left(T_s-T_{ave}\left(x\right)\right)}\left.\frac{\partial T}{\partial z}\right|_w \tag{4}$$

$$Nu = \frac{h\left(x\right)D_h}{\lambda} = \frac{2H}{T_s - T_{ave}}\frac{\partial T}{\partial z}\bigg|_w \tag{5}$$

In the equation, D_h is the characteristic dimension of the nanochannel, where $D_h = 2H$ for a smooth channel and $D_h = 2H + 2h$ for a rough channel. λ represents the thermal conductivity of the working fluid, and $\partial T/\partial z|_w$ corresponds to the fluid temperature gradient at the liquid-solid interface. T_s signifies the temperature of the solid boundary.

$$l_k = \frac{\Delta T}{\frac{\partial T}{\partial z}\big|_w} \tag{6}$$

Within this formula, l_k is the thermal slip length, and ΔT denotes the thermal slip at the liquid-solid interface, which is defined as the discrepancy between the fluid temperature and the boundary temperature. ΔT is determined by fitting the fluid temperature profile in the core flow region using a fourth-order polynomial, then extrapolating this fit to the liquid-solid interface.

As shown in Fig. 6a,b. the thermal slip length decreases markedly with increasing wettability and roughness, while the *Nu* number exhibits an increasing trend. This indicates a significant enhancement of interfacial heat transfer in the nanochannel. When the wettability of a smooth nanochannel changes from weak to strong, the thermal slip length decreases by 50.76%, and the corresponding *Nu* number increases by 35.09%. This demonstrates that more hydrophilic surfaces induce stronger solid–fluid interactions and thus more efficient heat exchange. Under weak wettability conditions, increasing roughness from Case 1 to Case 4 reduces the thermal slip length by 37.06% and increases *Nu* number by 31.24%. In contrast, under strong wettability conditions, the thermal slip length decreases by 56.45% and *Nu* number increases by 53.81%. The comparison indicates that roughness-induced heat transfer enhancement is more pronounced under strong wettability than under weak wettability. The thermal slip length of Case $1 - \alpha = 1$ is smaller than that of Case $4 - \alpha = 0.5$, while its local *Nu* number is higher. This confirms that, in the present study, the influence of wettability on heat transfer is much greater than that of surface roughness, with wettability playing a dominant role. This behavior results from the specific selection of the wettability tuning factor and roughness magnitude in this work.

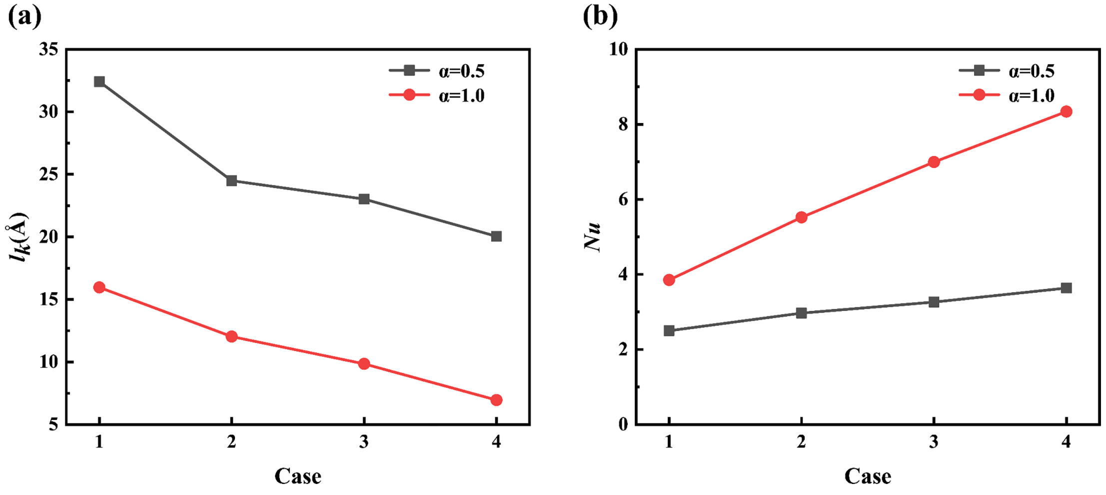

Figure 6: Under different wettability and roughness conditions (**a**) Thermal slip length; (**b**) *Nu* number.

3.2 *Effect of Wettability and Rough Morphology Coupling on Flow Characteristics in Nanochannels*

Fluid velocity profiles within nanochannels represent a critical parameter for describing fluid transport dynamics. Fig. 7 shows the two-dimensional velocity distributions along the flow direction for different models. Under all models, the fluid flow in the nanochannels is fully developed, with only minor velocity gradients along the x direction. In contrast, pronounced velocity gradients appear near the solid–liquid interface along the z direction. For the same roughness configuration, increasing wettability reduces the area of high-velocity regions. This is because enhanced interfacial hydrophilicity restricts the motion of fluid atoms, leading to a slower development of the velocity field. For the same wettability, higher wall roughness also decreases the area of high-velocity regions. This indicates that increasing the density of surface nanopillar arrays promotes stronger confinement of argon atoms near the solid surface, thereby hindering fluid flow.

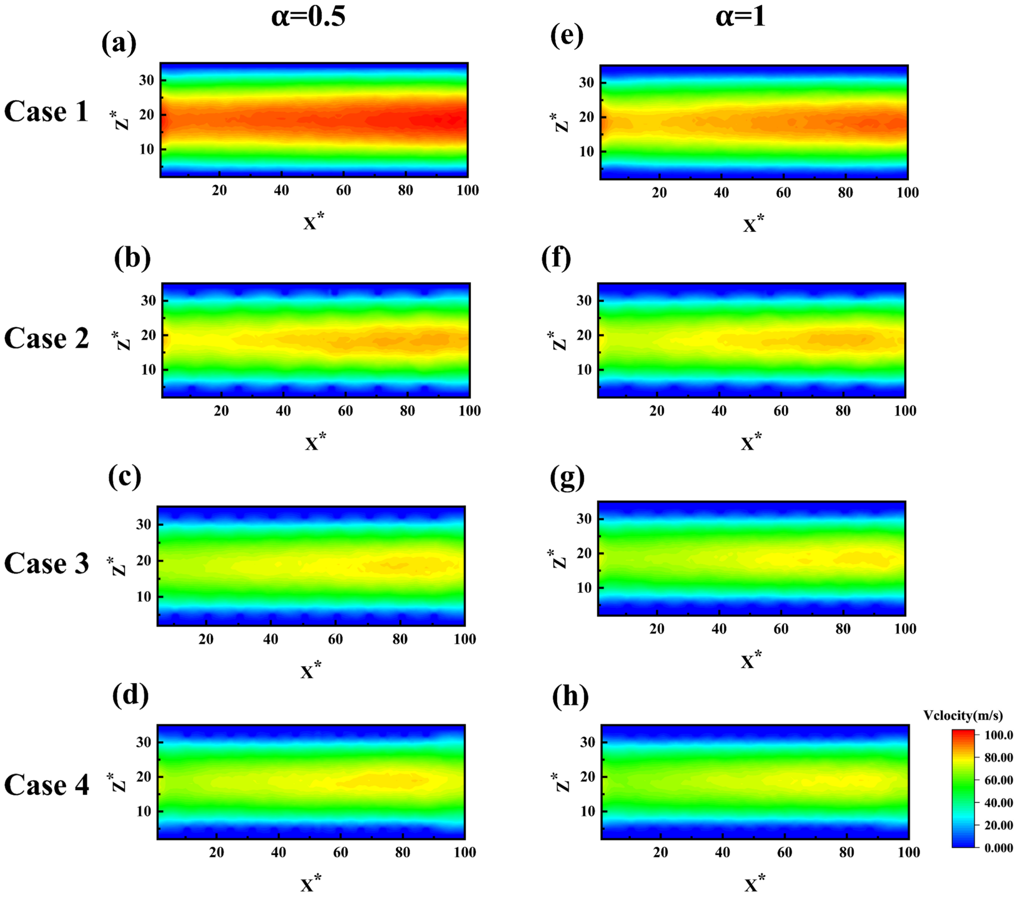

Figure 7: Two-dimensional velocity distributions; (**a**–**h**) nanochannels with different roughness and wettability.

To further analyze variations in flow characteristics within the nanochannel, the development of the velocity field is quantitatively examined. Fig. 8 illustrates one-dimensional velocity profiles along the z-axis at distinct x locations. The maximum velocity in Case 1 − $\alpha = 0.5$ is the highest among all cases, reaching approximately 104.08 m/s (1.04 Å/ps). The maximum velocity in Case 1 − $\alpha = 1$ is 91.45 m/s, while that in Case 2 −$\alpha = 0.5$ is 87.57 m/s. For these three models, changes in roughness have a more pronounced effect on the flow velocity. The maximum velocity in Case 3 − $\alpha = 0.5$ is 81.67 m/s, that in Case 3 − $\alpha = 1$ is 79.01 m/s, and that in Case 4 −$\alpha = 0.5$ is 80.18 m/s. For these models, variations in wettability have a greater influence on the flow velocity. Therefore, when both wettability and rough surface structures vary simultaneously, their effects on nanochannel flow are not consistent.

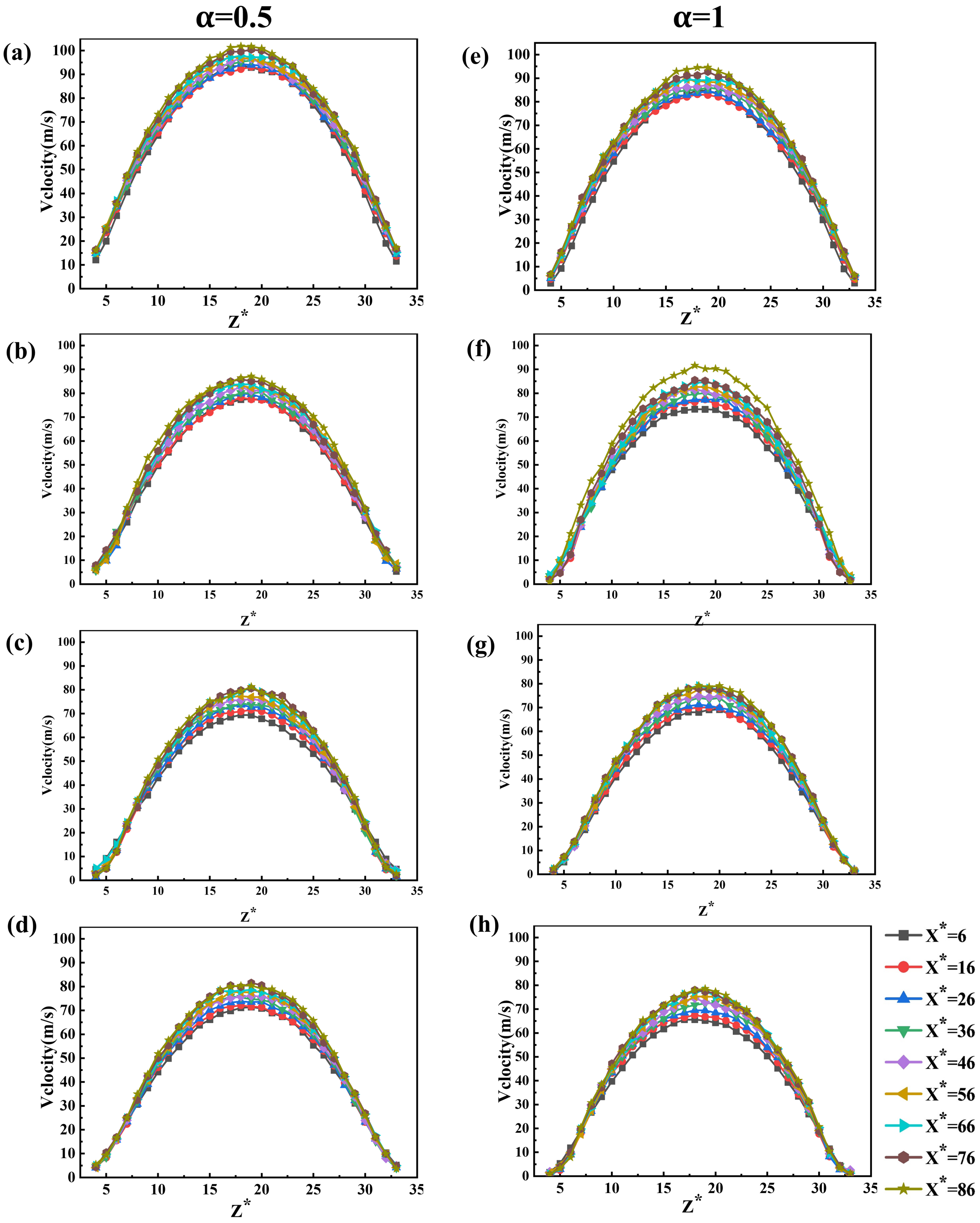

Figure 8: Velocity distributions along the z direction at different x positions; (**a**–**h**) nanochannels with different roughness and wettability.

Velocity profiles along the z-axis at $X^* = 85.5$ across all simulation models are presented in Fig. 9. Combined with Fig. 5a. it becomes clear that the evolution trend of the velocity field is the inverse of that observed for the temperature field. While increased wettability and surface roughness reduce interfacial thermal resistance and enhance heat transfer, they also impose a certain degree of resistance to fluid flow. For the same wettability, clear differences in the core-region velocity are observed under different roughness conditions. In contrast, in the near-wall region, the velocity differences are relatively small due to confinement by surface roughness. This indicates that the influence of different rough structures on the velocity field is mainly manifested in the core flow region. From Figs. 8 and 9, it is evident that the fluid velocity at the wall is not zero, confirming the existence of velocity slip at the solid–liquid interface.

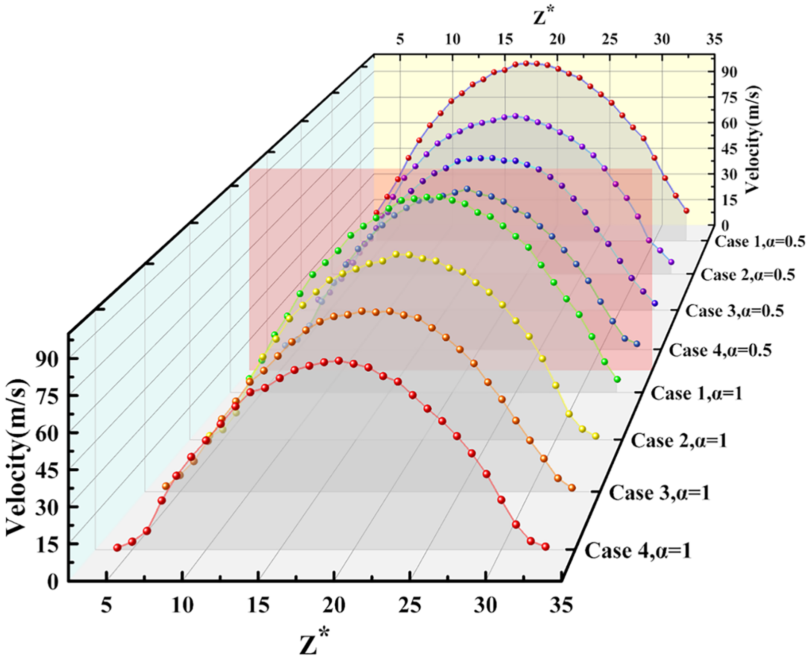

Figure 9: Velocity distributions of different models at X* = 85.5.

To further investigate the impacts of wettability-roughness synergy on flow impedance within nanochannels, the velocity slip length and relative friction coefficient are computed to describe interfacial microscale dynamics. The corresponding definitions are given in Eqs. (7) and (10) [29]. Here, l_s denotes the velocity slip length, f is the friction coefficient, and f^* represents the relative friction coefficient. The calculation range for both ls and f^* is selected from X* = 45 to X* = 85.

$$l_s = \frac{\Delta u_s}{\left.\frac{\partial u_s}{\partial z}\right|_w} \tag{7}$$

In the equations, Δu_s and $\partial u_s/\partial z|_w$ are obtained by fitting the velocity distribution in the core flow region with a second-order polynomial function and extrapolating it to the solid–liquid interface.

$$f = \frac{\frac{\Delta p}{L_x} D_h}{\frac{1}{2}\rho u_m^2} \tag{8}$$

$$f = \frac{F_{ext} D_h}{\frac{1}{2} m u_m^2} \tag{9}$$

In the equations, ΔP is the pressure difference along the flow direction, L_x is the nanochannel length, and um is the mean fluid velocity. Since fluid flow in the nanochannel is driven by a constant external force

F_{ext} applied along the x direction, $NF_{ext} \approx (\Delta P)A$, where N represents the total number of fluid atoms and A denotes the cross-sectional area of the channel. On this basis, the friction coefficient can be simplified as presented in Eq. (9).

$$f^* = \frac{f}{f_0} \tag{10}$$

The calculated results are shown in Fig. 10a. Increasing wettability and roughness both reduce the velocity slip length, which is consistent with the velocity distribution results. Under weak wettability conditions, increasing roughness from Case 1 to Case 4 decreases the velocity slip length by 119.44% and increases the relative friction coefficient by 29.51%. Under strong wettability conditions, the velocity slip length decreases by 248.15% and the relative friction coefficient increases by 37%, indicating that roughness has a more pronounced effect on velocity slip under strong wettability.

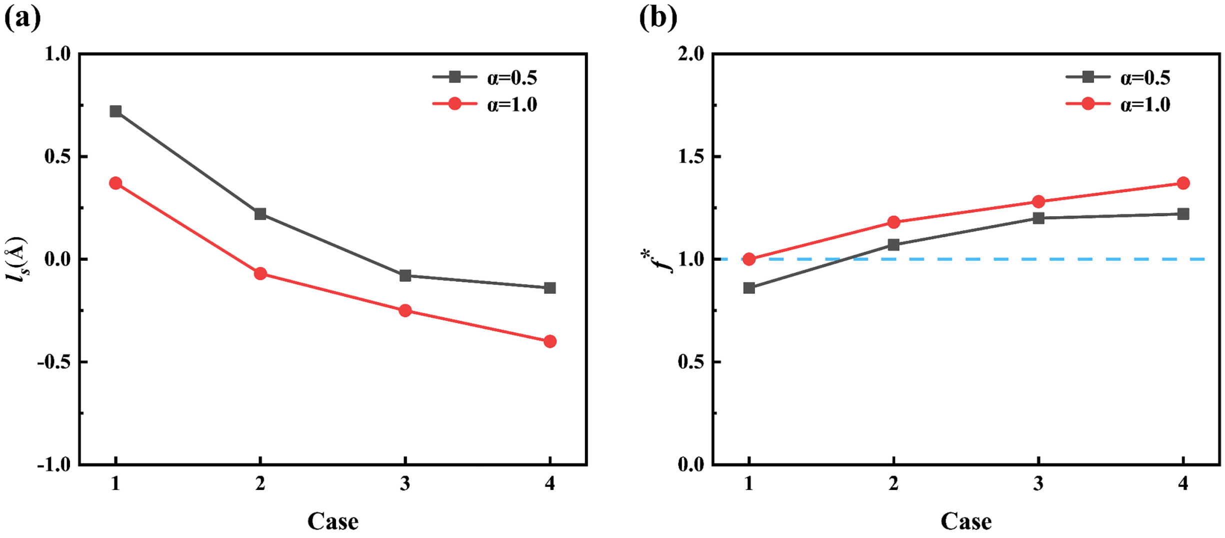

Figure 10: (**a**) Velocity slip length; (**b**) relative friction coefficient. The blue dashed line denotes the relative friction coefficient of the smooth nanochannel under strong wettability.

As depicted in Fig. 10b, the relative friction coefficient of Case $2 - \alpha = 0.5$ is 1.07, which is higher than that of Case $1 - \alpha = 1$. This differs from the heat transfer results, where wettability plays a dominant role. Both surface wettability and roughness impose significant resistance to fluid flow in nanochannels. This is because stronger surface hydrophilicity and denser nanopillar arrays hinder the motion of fluid atoms near the interface. In this study, the combined effects of surface wettability and roughness on flow resistance in nanochannels show no obvious dominant-subordinate relationship.

3.3 Overall Heat Transfer Performance

To enable a direct comparison of the synergistic impacts of surface wettability and roughness on thermal transport and flow impedance in nanochannels, the *Nu* number and relative friction coefficient of a smooth nanochannel under high wettability conditions are designated as baseline values. The variation ratios under other conditions are illustrated in Fig. 11a. Clearly, Case $4 - \alpha = 1$ exhibits the largest increases in both *Nu* number and relative friction coefficient, reaching 117% and 49%, respectively. High surface wettability and roughness promote enhanced thermal transport but impede the reduction of flow drag. Although Case $1 - \alpha = 0.5$ has the lowest flow resistance, its *Nu* number decreases by 14% relative to the reference value.

Compared with Case 3 − α = 1, Case 4 − α = 1 shows only a 3% increase in flow resistance, while Nu number increases by 35%. This indicates that increasing the nanopillar array from Case 3 to Case 4 slightly impedes fluid flow but significantly enhances convective heat transfer.

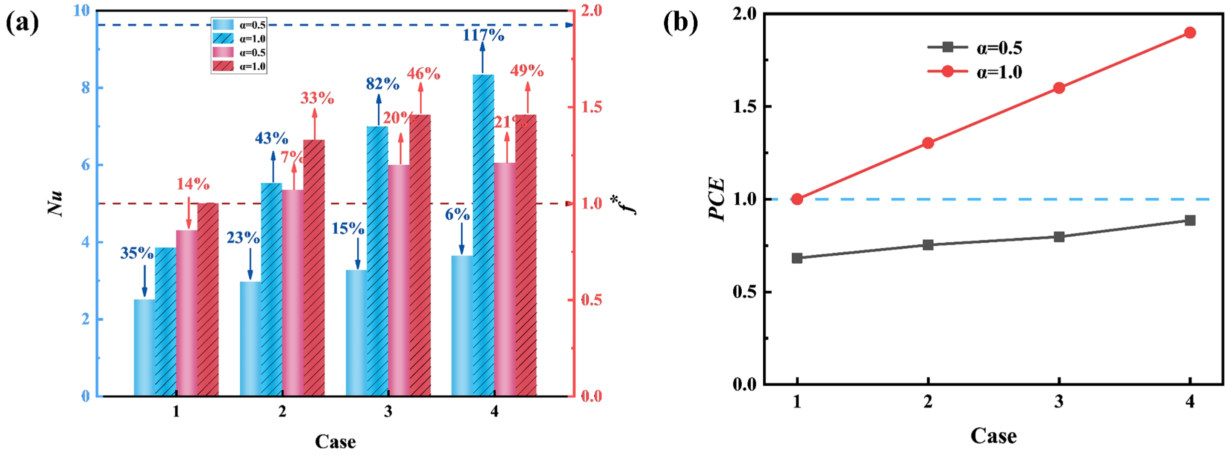

Figure 11: (**a**) Impacts of wettability and roughness on thermal heat and flow resistance; (**b**) Performance evaluation criterion of all cases.

The overall thermal transport performance of the nanochannels is assessed via the Performance Evaluation Criterion (PEC), defined in Eq. (11) [41,42], and the results are presented in Fig. 11b. The PEC values differ markedly with wettability, and all models under weak wettability exhibit PEC values lower than unity. Combined with Fig. 11a, Case 1 − α = 1 shows a 6% higher Nu number and a 21% lower relative friction coefficient than Case 4 − α = 0.5, indicating that, in this study, improving surface wettability has a greater impact on overall heat transfer performance than increasing surface roughness. From a lateral comparison, for the same wettability, increasing roughness exerts a stronger enhancement effect on heat transfer than its increment effect on flow resistance, leading to higher PEC values with increasing roughness. This demonstrates that the selected nanopillar arrays in this study provide favorable overall heat transfer performance.

$$\mathrm{PEC} = \frac{Nu/Nu_0}{(f/f_0)^{1/3}} \tag{11}$$

In the equation, Nu_0 and f_0 denote the parameters of the smooth nanochannel under strong wettability.

Finally, the interaction energy between wall platinum atoms and fluid argon atoms is calculated to elucidate the microscopic mechanism from an atomic interaction perspective. The results are shown in Fig. 12. Platinum atoms and argon atoms attract each other; therefore, the interaction energy is negative [9]. With increasing wettability and surface roughness, the interaction energy is enhanced. Under strong wettability conditions, the solid–liquid interaction energy of Case 1 − α = 1 is −2993.68, while that of Case 4 − α = 1 reaches −3941.51, corresponding to an increase of 20.01%. In contrast, for smooth nanochannels, the interaction energy increases by 148.64% when wettability changes from weak to strong.

As indicated by Fig. 12, wettability has a more pronounced effect on interaction energy than surface roughness, which is consistent with the above conclusions that wettability plays a dominant role in heat transfer enhancement in this study. More hydrophilic and rougher solid surfaces significantly increase solid–liquid atomic interaction energy and thereby strengthen interfacial heat transfer in nanochannels.

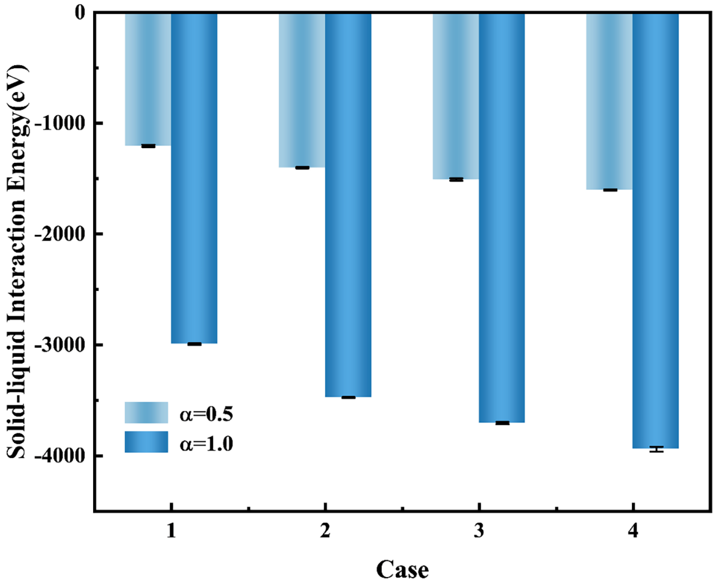

Figure 12: Solid-liquid interaction energy of all cases.

4 Conclusions

In the present work, MD simulations are utilized to examine the synergistic impacts of surface wettability and rough nanostructures on thermal transport and flow resistance within nanochannels. Key conclusions from this investigation are outlined below.

(1) Increasing surface hydrophilicity and roughness density significantly enhances heat transfer in nanochannels, while the fluid flow is correspondingly impeded.

(2) For the strong and weak wettability conditions and progressively denser nanopillar arrays considered in this study, wettability plays a dominant role in heat transfer enhancement. In terms of flow resistance, the effects of wettability and surface roughness are comparable and difficult to distinguish the dominance.

(3) Under the same wettability condition, the PEC increases with increasing roughness. This indicates that the heat transfer enhancement induced by increased roughness outweighs the associated increase in flow resistance, demonstrating that the designed nanopillar arrays exhibit excellent overall heat transfer performance.

Acknowledgement: None.

Funding Statement: This work was supported by supported by Yunnan Fundamental Research Projects (202301AT070469), National Natural Science Foundation of China under Contract (No. 32460452), and supported by Yunnan Major Research Projects (No. 202502AB080016).

Author Contributions: We appreciate the contributions of co-authors. Yanfeng Li: methodology, formal analysis, investigation, writing—original draft. Xiaohui Zhang: conceptualization, resources, writing—review & editing, funding acquisition. Luyang Chen: supervision, project administration. Shan Qing: software. Rong Chen: funding acquisition, supervision, project administration. All authors reviewed and approved the final version of the manuscript.

Availability of Data and Materials: Data available on request from the authors.

Ethics Approval: Not applicable.

Conflicts of Interest: The authors declare no conflicts of interest.

Nomenclature

L	Length of the coordinate axis, [Å]
S	Diameter, [Å]
l	Distance between pillars, [Å]
h	Pillar height, [Å]
H	Upper boundaries, [Å]
T	Temperature, [K]
u_x	Local average velocity, [m/s]
Nu	Nusselt
l_k	Thermal slip length, [Å]
$h(x)$	Local convective heat transfer coefficient
D_h	Characteristic dimension
l_s	Velocity slip length, [Å]
f	Friction coefficient
u_s	Fluid velocity at the interface, [m/s]
F	External force, [pN]
N	Number of atoms
m	Mass, [kg]

Greek symbols

δ	Lattice constant, [Å]
ε	Energy parameter
σ	Distance parameter
λ	Thermal conductivity
ρ	Density, [kg/m^3]
ΔT	Thermal slip at the liquid-solid, [K]
ΔP	Pressure difference along the flow direction, [Pa]

Subscripts

ave	Averaged value
w	Wall
ext	External
0	Reference value

Abbreviations

MD	Molecular dynamics
FCC	Face-centered cubic
PEC	Performance Evaluation Criterion

References

1. Fathi M, Heyhat MM, Zabetian Targhi M, Bigham S. Bifurcated divergent microchannel heat sinks for enhanced micro-electronic cooling. Int Commun Heat Mass Transfer. 2023;146:106868. doi:10.1016/j.icheatmasstransfer.2023.106868.
2. Van Erp R, Soleimanzadeh R, Nela L, Kampitsis G, Matioli E. Co-designing electronics with microfluidics for more sustainable cooling. Nature. 2020;585(7824):211–6. doi:10.1038/s41586-020-2666-1.
3. Wu R, Hong T, Cheng Q, Zou H, Fan Y, Luo X. Thermal modeling and comparative analysis of jet impingement liquid cooling for high power electronics. Int J Heat Mass Transfer. 2019;137:42–51. doi:10.1016/j.ijheatmasstransfer.2019.03.112.

4. Li Y, Zhang F, Sunden B, Xie G. Laminar thermal performance of microchannel heat sinks with constructal vertical Y-shaped bifurcation plates. Appl Therm Eng. 2014;73(1):185–95. doi:10.1016/j.applthermaleng.2014.07.031.
5. Ferhi M, Djebali R. Multi-objective optimization of microporous heat exchangers: a sensitivity analysis and response surface methodology. Case Stud Therm Eng. 2025;73:106653. doi:10.1016/j.csite.2025.106653.
6. Guo ZY, Li ZX. Size effect on microscale single-phase flow and heat transfer. Int J Heat Mass Transfer. 2003;46(1):149–59. doi:10.1016/S0017-9310(02)00209-0.
7. Zhang L, Cui Z, Cao Q, Liang S, Liu Y, Ma X. Molecular dynamics study of spontaneous capillary flow and heat transfer in nanochannels. Int Commun Heat Mass Transfer. 2022;137:106228. doi:10.1016/j.icheatmasstransfer.2022.106228.
8. Liu X, Zong X, Xue S, Liu H, He M. Molecular structure and transport of ionic liquid confined in asymmetric graphene-coated silica nanochannel. J Mol Liq. 2022;345:117869. doi:10.1016/j.molliq.2021.117869.
9. Song Z, Shang X, Cui Z, Liu Y, Cao Q. Investigation of surface structure-wettability coupling on heat transfer and flow characteristics in nanochannels. Appl Therm Eng. 2023;218:119362. doi:10.1016/j.applthermaleng.2022.119362.
10. Markvoort AJ, Hilbers PAJ, Nedea SV. Molecular dynamics study of the influence of wall-gas interactions on heat flow in nanochannels. Phys Rev E. 2005;71(6):066702. doi:10.1103/PhysRevE.71.066702.
11. Ge S, Gu Y, Chen M. A molecular dynamics simulation on the convective heat transfer in nanochannels. Mol Phys. 2015;113:703–10. doi:10.1080/00268976.2014.970593.
12. Guo Z, Zhao TS, Shi Y. Temperature dependence of the velocity boundary condition for nanoscale fluid flows. Phys Rev E. 2005;72(3):036301. doi:10.1103/PhysRevE.72.036301.
13. Zhang H, Zhang Z, Ye H. Molecular dynamics-based prediction of boundary slip of fluids in nanochannels. Microfluid Nanofluid. 2012;12(1–4):107–15. doi:10.1007/s10404-011-0853-y.
14. Song FQ, Wang JD. Investigation of influence of wettability on poiseuille flow via molecular dynamics simulation. J Hydrodyn. 2010;22(4):513–7. doi:10.1016/S1001-6058(09)60083-4.
15. Rashidi MM, Ghahremanian S, Toghraie D, Roy P. Effect of solid surface structure on the condensation flow of argon in rough nanochannels with different roughness geometries using molecular dynamics simulation. Int Commun Heat Mass Transfer. 2020;117:104741. doi:10.1016/j.icheatmasstransfer.2020.104741.
16. Zhang Y. Effect of wall surface roughness on mass transfer in a nano channel. Int J Heat Mass Transfer. 2016;100:295–302. doi:10.1016/j.ijheatmasstransfer.2016.04.097.
17. Yao S, Wang J, Liu X. Influence of nanostructure morphology on the heat transfer and flow characteristics in nanochannel. Int J Therm Sci. 2021;165:106927. doi:10.1016/j.ijthermalsci.2021.106927.
18. Guo WQ, Deng JW, Wang BB. Molecular dynamics simulations on heat transport of nanoconfined water under electric fields: effect of nanochannel size. J Phys Chem B. 2025;129(1):348–59. doi:10.1021/acs.jpcb.4c06213.
19. Karimi R, Marzban A, Toghraie D. The molecular dynamics study of the thermal behavior of argon flow in a nanochannel with changes in nanochannel cross-section. Results Phys. 2025;70:108143. doi:10.1016/j.rinp.2025.108143.
20. Cao BY, Sun J, Chen M, Guo ZY. Molecular momentum transport at fluid-solid interfaces in MEMS/NEMS: a review. Int J Mol Sci. 2009;10(11):4638–706. doi:10.3390/ijms10114638.
21. Kumar P, Pathak M. Droplet formation under wall slip in a microfluidic T-junction. J Mol Liq. 2022;345:117808. doi:10.1016/j.molliq.2021.117808.
22. Toghraie Semiromi D, Azimian AR. Nanoscale Poiseuille flow and effects of modified Lennard–Jones potential function. Heat Mass Transfer. 2010;46(7):791–801. doi:10.1007/s00231-010-0624-4.
23. Kapitza PL. Heat transfer and superfluidity of helium II. Phys Rev. 1941;60(4):354–5. doi:10.1103/PhysRev.60.354.
24. Ma M, Zhang XH, Xiong C, Huang XY, Chen LY, Qing S, et al. Microscopic mechanisms of thermal transport at the SiO_2-water interface under the influence of wettability: a molecular dynamics study. Chem Phys. 2025;595:112700. doi:10.1016/j.chemphys.2025.112700.
25. Lin T, Li J, Quan X, Cheng P. A molecular dynamics investigation on effects of nanostructures on thermal conductance across a nanochannel. Int Commun Heat Mass Transfer. 2018;97:118–24. doi:10.1016/j.icheatmasstransfer.2018.05.025.

26. Zhang P, Liu Z, Liu X, Liu G. Electrokinetic energy conversion via nanochannel roughness engineering. Desalination. 2025;616:119402. doi:10.1016/j.desal.2025.119402.
27. Li S, Lu C, Zhang C, Li Z, Zhao J, Chen J, et al. Modeling and investigation of fluid flow affecting thermal boundary conductance at the solid-fluid interface. Int J Heat Mass Transfer. 2023;213:124333. doi:10.1016/j.ijheatmasstransfer.2023.124333.
28. Miao S, Xia G, Zhou W, Shang H. Effect of wettability and surface roughness on flow and heat transfer characteristics in nanochannels. Phys Fluids. 2024;36(10):103613. doi:10.1063/5.0232006.
29. Yao S, Wang J, Liu X. Role of wall-fluid interaction and rough morphology in heat and momentum exchange in nanochannel. Appl Energy. 2021;298:117183. doi:10.1016/j.apenergy.2021.117183.
30. Qin S, Chen Z, Li W, Ma A, Xie L. Effect of wall wettability coupled nanostructure on fluid molecular ordering near wall and flow heat transfer in asymmetric nanochannels. Int Commun Heat Mass Transfer. 2024;159:108070. doi:10.1016/j.icheatmasstransfer.2024.108070.
31. Huang X, Liu R, Liu Z. Evaporation of ultra-thin water film on hot spot with nanopillar array. Int J Therm Sci. 2022;182:107807. doi:10.1016/j.ijthermalsci.2022.107807.
32. Lee E, Zhang T, Yoo T, Guo Z, Luo T. Nanostructures significantly enhance thermal transport across solid interfaces. ACS Appl Mater Interfaces. 2016;8(51):35505–12. doi:10.1021/acsami.6b12947.
33. Plimpton S. Fast parallel algorithms for short-range molecular dynamics. J Comput Phys. 1995;117(1):1–19. doi:10.1006/jcph.1995.1039.
34. Chambliss A, Frankin J. A magnetic velocity verlet method. Am J Phys. 2020;88):1075–82. doi:10.1119/10.0001876.
35. Humphrey W, Dalke A, Schulten LK. VMD: visual molecular dynamics. J Mol Graph. 1996;14:33–8. doi:10.1016/0263-7855(96)00018-5.
36. Song Z, Cui Z, Cao Q, Liu Y, Li J. Molecular dynamics study of convective heat transfer in ordered rough nanochannels. J Mol Liq. 2021;337:116052. doi:10.1016/j.molliq.2021.116052.
37. Wang M, Sun H, Cheng L. Investigation of convective heat transfer performance in nanochannels with fractal cantor structures. Int J Heat Mass Transfer. 2021;171:121086. doi:10.1016/j.ijheatmasstransfer.2021.121086.
38. Chakraborty P, Ma T, Cao L, Wang Y. Significantly enhanced convective heat transfer through surface modification in nanochannels. Int J Heat Mass Transfer. 2019;136:702–8. doi:10.1016/j.ijheatmasstransfer.2019.03.053.
39. Marable DC, Shin S, Yousefzadi Nobakht A. Investigation into the microscopic mechanisms influencing convective heat transfer of water flow in graphene nanochannels. Int J Heat Mass Transfer. 2017;109:28–39. doi:10.1016/j.ijheatmasstransfer.2017.01.100.
40. Bagheri Motlagh M, Kalteh M. Investigating the wall effect on convective heat transfer in a nanochannel by molecular dynamics simulation. Int J Therm Sci. 2020;156:106472. doi:10.1016/j.ijthermalsci.2020.106472.
41. Tu J, Qi C, Li K, Tang Z. Numerical analysis of flow and heat characteristic around micro-ribbed tube in heat exchanger system. Powder Technol. 2022;395:562–83. doi:10.1016/j.powtec.2021.10.009.
42. Sun H, Liu Z, Xin G, Xin Q, Zhang J, Cao BY, et al. Thermal and flow characterization in nanochannels with tunable surface wettability: a comprehensive molecular dynamics study. Numer Heat Transf Part A Appl. 2020;78(6):231–51. doi:10.1080/10407782.2020.1788849.